Materials Science in Semiconductor Processing 162 (2023) 107505

Contents lists available at ScienceDirect

Materials Science in Semiconductor Processing

journal homepage: www.elsevier.com/locate/mssp

Modulating incident light for improved CO_2 photoreduction in freestanding silver bismuth iodide/nanocellulose films with exotic gold nanoparticles

Ming-Chung Wu [a,b,d,*], Yin-Hsuan Chang [a], Yi-Jing Lu [a], Kai-Chi Hsiao [a], Ting-Han Lin [a], Jia-Mao Chang [a], Kai-Hsiang Hsu [b], Jen-Fu Hsu [b,c,**], Kun-Mu Lee [a,b,d,***]

[a] Department of Chemical and Materials Engineering, College of Engineering, Chang Gung University, Taoyuan, 33302, Taiwan
[b] Division of Neonatology, Department of Pediatrics, Chang Gung Memorial Hospital at Linkou, Taoyuan, 33305, Taiwan
[c] School of Medicine, College of Medicine, Chang Gung University, Taoyuan, 33302, Taiwan
[d] Green Technology Research Center, Chang Gung University, Taoyuan, 33302, Taiwan

ARTICLE INFO

Keywords:
Silver bismuth iodide
CO_2 conversion
Photoreduction
Photocatalyst
Nanocellulose

ABSTRACT

In response to the severe climate change caused by significant carbon dioxide emissions, researchers have been exploring the conversion of CO_2 into carbon-based fuels through photocatalytic reactions inspired by photosynthesis. Particulate photocatalysts are known for their easy fabrication and diverse material configuration, with immobilization onto composite polymers enhancing reusability and practicality. In this study, we fabricated a novel freestanding photocatalyst composite film by immobilizing Ag_3BiI_6 (SBI) onto a nanocellulose (CNF) transparent film using a sequential process involving noble metal nanoparticle solutions and thermal evaporation of BiI_3. The effect of the sequence and composition of Au and SBI/CNF on the morphology, optical property, and CO_2 photoreduction performance was also investigated. The resulting SBI-Au/CNF film exhibited the highest photocatalytic activity for CO_2 reduction, achieving a CO yield of 31.96 μmol/g·h with high stability for long-term photocatalytic reactions lasting 72 h. This study demonstrates the potential of photocatalytic materials to mitigate climate change by converting CO_2 emissions into useful fuels.

1. Introduction

The increasing carbon dioxide emissions are a major contributor to global warming and severe climate change. Scientists are devoted to searching for a remedy to convert CO_2 into value-added fuel and alleviate the impacts of climate change. At present, inspired by the process of photosynthesis, the conversion of CO_2 into carbon-based fuels (CO, CH_4, etc.) can be realized by using solar energy to reduce CO_2 [1–5]. In addition to solving the CO_2 issue, CO_2 photoreduction can also realize artificial carbon cycling to solve the energy crisis [6–11]. However, the versatile routes for CO_2 reduction and the high dissociation energy of the C═O bond (750 kJ/mol) limit the conversion of CO_2 to a high energy-bearing product [12–15]. Also, the charge carrier migration efficiency caused by recombination sites remains a challenge to construct an efficient photocatalyst for CO_2 photoreduction or methane conversion [16,17]. To resolve the short lifetime and recombination of carriers in photocatalysis, heterostructure photocatalysis is established to prolong their lifetime and separation efficiency by an internal electrical field difference between an interface. It guides excited electrons transferring to the surface and forms an active site owing to their intimate contact [18]. On the other hand, noble-metal-free materials such as Ni_2P, sulfur- and chlorine-co-doped g-C_3N_4, In_2O_3, and NiS have been reported to be effective co-catalysis to construct a *S*-scheme photocatalysis with high photocatalytic activity for hydrogen production or CO_2 reduction [19–21].

Besides, the recyclability of used photocatalysts is also another critical issue. Particle-based photocatalysts face problems such as aggregation and difficulty in reuse, and they require stirring during the reaction. Immobilizing photocatalysts as thin films effectively overcomes these disadvantages [22–24]. Cellulose exhibits outstanding chemical stability, and nontoxicity, which is regarded as a candidate for next-generation sustainable materials [25–27]. Besides, the biodegradability and ecologically friendly cellulose will not cause secondary pollution to the environment [28–30]. Many studies have shown that

* Corresponding author. Department of Chemical and Materials Engineering, College of Engineering, Chang Gung University, Taoyuan, 33302, Taiwan.
** Corresponding author. Division of Neonatology, Department of Pediatrics, Chang Gung Memorial Hospital at Linkou, Taoyuan, 33305, Taiwan.
*** Corresponding author. Department of Chemical and Materials Engineering, College of Engineering, Chang Gung University, Taoyuan, 33302, Taiwan.
E-mail addresses: mingchungwu@cgu.edu.tw (M.-C. Wu), hsujanfu@cgmh.org.tw (J.-F. Hsu), kmlee@cgu.edu.tw (K.-M. Lee).

https://doi.org/10.1016/j.mssp.2023.107505
Received 16 February 2023; Received in revised form 30 March 2023; Accepted 5 April 2023
Available online 12 April 2023

cellulose may be an ideal supporter for photocatalysts [31,32]. Jiang et al. have fabricated film-based photocatalysts by supporting Ag/A-g_2O–ZnO particles on a cellulose-chitosan 3D nanofiber network. Ag_2O reacted with hydroxyl groups provide electrostatic interaction for ZnO to absorb onto the surface of Ag/Ag_2O [33]. Wu et al. demonstrated that cellulose nanofibers exhibit good compatibility for immobilizing TiO_2 due to the physical embedding of cellulose fiber. The hierarchical structure of cellulose nanofiber composite determining their physiochemical properties. The mechanical properties of CNF flms can be improved by embedding ceramic materials of TiO_2. By manipulating the morphology of TiO_2 from spherical shape to nanofiber, both crystallinity and mechanical strength of composite film can be effectively enhanced [34].

Currently, bismuth-based compounds have been seen as a potential candidate as photocatalysts due to their high visible light absorption ability, tunable bandgap, and suitable alignment of energy levels. Cs_2AgBiX_6 double perovskite nanocrystals with tunable absorption of visible light show a good performance in CO_2 photoreduction. The radiation recombination of photogenerated carriers can be reduced by tuning the halide compounds [35]. Zhang et al. have demonstrated the photodegradation of methylene blue by Ag_2BiI_5 thin films. The iodization of Ag-diffused BiI_3 resulted in uniform Ag_2BiI_5 thin films. The weak van der Waals interaction between the I–Bi–I layers tends to insert guest metallic layers in BiI_3 to form new compounds [36].

In this study, we demonstrate a new methodology for the fabrication of free-standing cellulose film through a facile vacuum filtration followed by a bismuth iodide thermal-evaporated processs, resulting in the formation of Ag_3BiI_6/cellulose nanofibers (SBI/CNF) film. The effect of the sequence and composition of varying precursor solutions on the morphology, optical property and CO_2 photoreduction performance was evaluated. The improved optical properties of SBI-Au/CNF film show high stability for long-term photocatalytic reactions and have CO reduction yield of 1500 μmol/g.

2. Experimental section

2.1. Synthesis of cellulose nanofibers and silver bismuth ioidide composite

Cellulose nanofibers hydrogel was prepared by TEMPO-mediated oxidation and further $NaBH_4$ post-reduction [34]. Pulp (Chung Hwa Pulp Corporation, laubholz bleached kraft pulp, LBKP) in the diluted HCl solution was heated to 100 °C for 2 h. After washed to neutral, 1.0 g of pulp was dispersed in 200 ml of deionized water, then 0.025 g of 2,2,6,6-Tetramethylpiperidine-1-oxyl (TEMPO, Acros, 98%) and 0.250 g of sodium bromide (NaBr, Acros, 99.5%) were dissolved in the mixture solution. Afterward, 0.08 mol of sodium hypochlorite (NaClO, Choneye, 12%) was gradually poured into the mixture solution, and the pH level was controlled at around 10.0 by dropping 0.5 M NaOH and/or $NaHCO_3$ for 24 h. To terminate the oxidation, few amounts of sodium thiosulfate pentahydrates ($Na_2S_2O_3{\cdot}5H_2O$, Acros, 99.5%) and ethanol were added. Subsequently, the post-reduction of sodium borohydride ($NaBH_4$, Acros, 98+%) was carried out to eliminate the undesirable functional group involving C6 aldehydes and C2/C3 ketones. Finally, CNF hydrogel was obtained after several times washing and collected by centrifugation.

For the preparation of the silver nanoparticle (Ag NPs) as SBI source, we followed the previous method [37,38]. 0.20 g of silver nitrate ($AgNO_3$, Sigma Aldrich, 99.9%), 4.0 ml of oleylamine (ACROS, 90%), and 100.0 ml of chlorobenzene (ACROS, 99.8%) were dissolved and placed in the four-neck flask. After well mixed, the solution were heated to 120 °C under continuous nitrogen purge for 1 h. It was then cooled to room temperature spontaneously. For the preparation of gold nanoparticles (Au NPs) as an Au source of SBI, 90.0 ml of $HAuCl_4{\cdot}3H_2O$ (ACROS, 99%) solution was first heated to be boiling under nitrogen purge. 1.8 ml of sodium citrate dehydrate (ECHO CHEMICAL CO. LTD, 99.5%) was injected into a boiling solution and further reacted for 10 min. After cooling, Au NPs were obtained [39].

The sequential reaction of SBI/CNF composite film was divided into two sections. The first section is to prepare the Au NPs, Ag NPs, and the mixture of Au/Ag NPs loaded CNF film, respectively. 0.05 wt% CNF hydrogel was loaded onto a hydrophilic membrane filter via suction filtration. Au, Ag, and Au/Ag mixture solutions were added separately and notated Au/CNF, Ag/CNF, and Ag/Au/CNF film. For easily peeling off films, these films were transferred to acetone for 5 min, and further dried in a vacuum for 10 min. The freestanding and flexible films were obtained. In the second section, various as-prepared films were attached to the top glass dish and BiI_3 was placed in the bottom of the glass dish, further heated at 200 °C for 30 min, and loaded onto films by thermal evaporation deposition. Subsequently, BiI_3-loaded films were transferred to an oven for thermal annealing at different temperatures for 10 min, approaching the SBI formation.

2.2. Materials characterization

The morphologies of monodispersed Ag and Au NPs were observed by Spherical-aberration Corrected Field Emission Transmission Electron Microscope (JEOL, JEM-ARM200FTH, Japan). The crystal structure of SBI was analyzed by an X-ray diffractometer (Bruker, D2 phaser with Xflash 430, Germany) with CuKα radiation at 50.0 kV and 300.0 mA. The optical property was measured by UV–vis spectrophotometer equipped with an integral sphere model (Jasco, V-650, Japan) in the wavelength range of 400–900 nm. The surface morphology of SBI composite films was observed by field-emission scanning electron microscopy (Hitachi, SU8010, Japan).

2.3. Photocatalytic experiment

For the photocatalytic CO_2 reduction, SBI films were attached to an inner side of an quartz-made reactor whose volume is about 560 ml. To prepare pure CO_2 gas, 3.0 g sodium bicarbonate was dissolved in 300.0 ml of deionized water in the reactor and purged under continuous N_2 gas flow for 30 min to remove the air. The CO_2 and H_2O gases were generated through the addition of 3.60 ml of hydrochloric acid (ACROS, 37%) to initiate a neutral reaction. Six pieces of the UV-B lamp (Sankyo Denki, G8T5 E, λ_{max} ~312 nm, 8.0 W) were placed around the reactor at a distance of 5.0 cm. At specified intervals, a 1.0 ml of the gas-phase product was sampled using a gas-tight syringe (Valco Instruments Company Inc), and the concentration of gas samples involving CO_2 and CO was determined by gas chromatograph (Shimazhu, Nexis GC-2030, Japan) equipped with barrier ionization discharge detector.

3. Results and discussion

For the sequential reaction of SBI, the quality of the developed precursor, Ag NPs and Au NPs, is important in obtaining high-quality SBI composite films. Fig. S1 shows the morphology and optical property of the as-synthesized precursor of Ag and Au NPs. The corresponding TEM images in Fig. S1(a) and **(d)** show the representative nanoparticles of Ag NPs and Au NPs. According to the TEM images, Ag NPs and Au NPs are well separated and have sphere-like morphology in the scale of 4–20 and 6–20 nm diameters, respectively. Fig. S1(b) and **(e)** show histograms corresponding to the size distribution obtained by TEM. The histogram presents Gaussian distribution with average diameters of 10.08 nm for Ag NPs and 13.77 nm for Au NPs. The homogenous size distribution facilitates the second step reaction of vapor/solid reaction between the reactants of metal NPs and BiI_3, which will be described in the next paragraph. Fig. S1(c) and **(f)** show the absorption spectra of the synthesized Ag NPs and Au NPs. The broad absorption peak at 415 and 523 nm is associated with the surface plasmon resonance effect from nanosized Ag and Au NPs.

In terms of two phases reaction, liquid/solid or gas/solid, immobilization of catalysts is a critical issue in improving recycling and reuse. As a result, cellulose nanofiber (CNF), exhibiting eco-friendly and high

permeability of gases, is selected as a substrate to hold the catalyst and construct a free-standing SBI/CNF composite film. The fabrication process of free-standing SBI/CNF composite film involves a two-step process and sequential reaction, as illustrated in Fig. 1. Three-typed free-standing composite films with different architectures are prepared through a facile vacuum filtration by adjusting the sequence and composition of varying precursor solutions. Fig. 1(a) shows the photographs of CNF, Ag NPs, Au NPs solution. The pronounced Tyndall effect of colloidal solutions of Ag and Au NPs again reveals that the synthesized NPs disperse with mere aggregation, consistent with Fig. S1, in the solvent system. Light management in photo-driven catalysts influences photocatalytic performance, especially for the type of thin film catalyst. The sequential reaction of SBI is deposited onto free-standing CNF films with different architectures, SBI/CNF, SBI/Au/CNF and SBI-Au/CNF, to manipulate the light scattering and carrier extraction effect from exotic Au NPs. The as-prepared CNF films are obtained from the vacuum filtration process of CNF solution. The free-standing film further serves as a substrate to hold the precursor of SBI, namely Ag NPs, and the co-catalyst/light scattering layer, Au NPs. Except for the control architecture of SBI/CNF, two different architectures, SBI/Au/CNF and SBI-Au/CNF, are designed to investigate the light scattering effect and lateral communication of carriers from exotic Au NPs as shown in Fig. 1(b). Fig. 1 (b-1) to **(b-3)** demonstrate the deposition of reactants, Ag/CNF, Ag/Au/CNF, and Ag–Au/CNF, for SBI sequential reaction. After that, bismuth iodide is thermal-evaporated onto the as-prepared reactants. A driving force from thermal energy is applied to accelerate the reaction and finish the sequential reaction of SBI, as shown in Fig. 1(c). The microstructure of SBI/CNF composite films is shown in Fig. 1(d). The pristine SBI layer is deposited onto the CNF film (the first illustration) for the control film. For target films, the Au NPs are sandwiched between CNF film and SBI layer (the second illustration) or Au NPs are emerged into the SBI film (the third illustration).

To confirm that thermal-evaporated BiI_3 is successfully converted into SBI, the various SBI/CNF composite films are characterized using X-ray diffractometer (XRD). The results are shown in Fig. 2(a). The diffraction peaks at 2θ of 15.5°, 15.9°, and 22.2° are indexed as I_α (triclinic) and I_β (monoclinic) phases of cellulose due to their allomorph. For the various SBI/CNF composite films, the typical diffraction peak of Ag_3BiI_6, observed at 2θ of 13.5°, 29.5°, 32.1°, 39.5°, and 41.7°, reveals clear evidence of a transformation from BiI_3 into Ag_3BiI_6 after finishing the sequential reaction route. A characteristic peak at nearly 38.0° represents the residual Ag NPs in control of SBI/CNF composite film. In comparison, the similar peaks in the spectrum of target films of SBI/Au/CNF and SBI-Au/CNF are indicative of either residual Ag NPs or Au NPs, which are not involved in the SBI sequential reaction. To realize the correlation between SBI and annealing temperature, the SBI-Au/CNF with the most pronounced SBI peaks in target films is further thermal annealed for 30 min at a temperature from 100 °C to 160 °C. The corresponding XRD patterns are shown in Fig. 2(b). Based on the XRD pattern, the intensity of SBI peaks climb as the annealing temperature increases, and the intensity obviously inflects as the further temperature increases to 160 °C. That indicates the SBI in the composite film has the highest crystallinity as the post-annealing is carried out at 140 °C for 30 min. As a result, further discussion is based on the optimized annealing

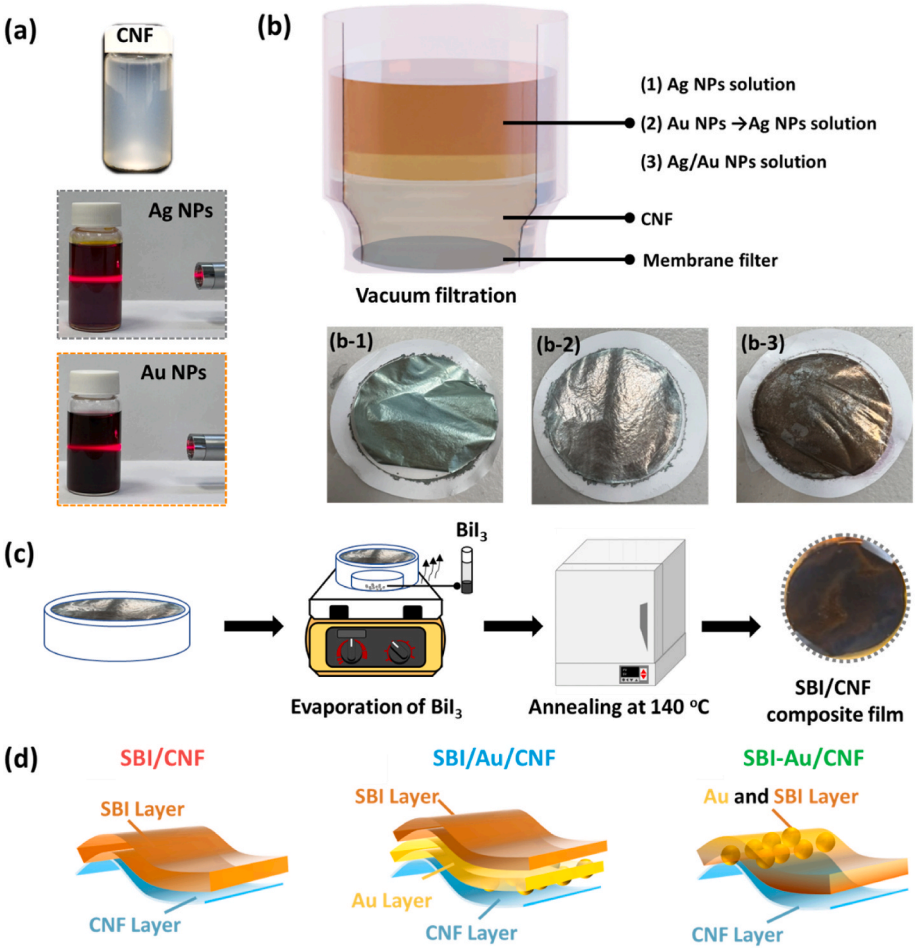

Fig. 1. Appearance of reactants for the sequential reaction of SBI: **(a)** digital photograph of the CNF, Ag NPs, and Au NPs solutions and **(b)** fabrication and digital photographs of the free-standing composite films from the first step, **(b-1)** Ag/CNF, **(b-2)** Ag/Au/CNF, **(b-3)** Ag–Au/CNF. Schematic illustration of SBI/CNF composite films: **(c)** second step of thermal-evaporated BiI_3 for the SBI/CNF composite films and **(d)** architectures of three-typed free-standing SBI/CNF composite films.

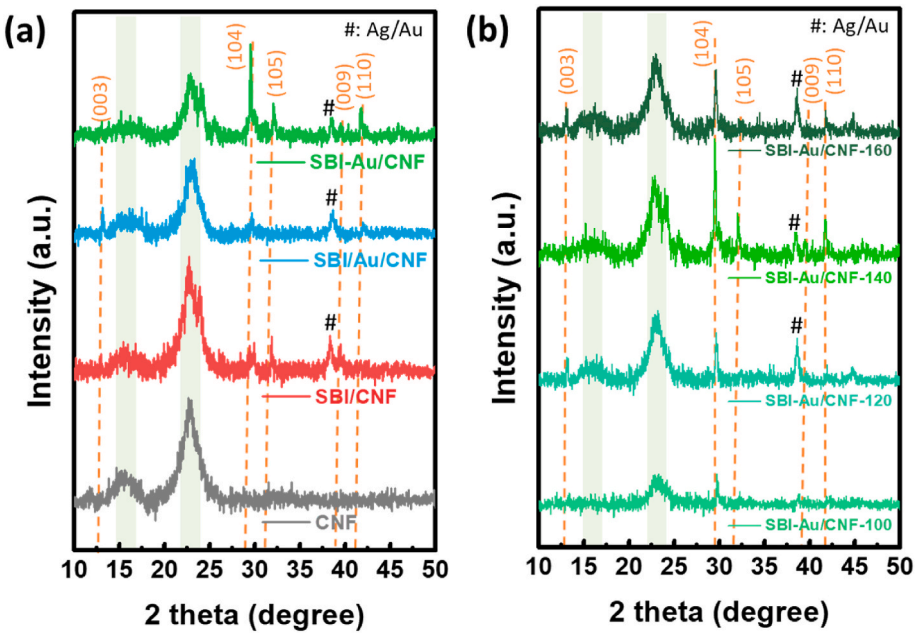

Fig. 2. Characterization of crystal structure: XRD pattern of **(a)** CNF, SBI/CNF, SBI/Au/CNF, and SBI-Au/CNF composite films and **(b)** SBI-Au/CNF with different annealing temperature.

condition in all SBI/CNF composite films.

In addition to crystal structure and crystallinity of the SBI composite films, surface morphology plays an influential role in communication of reactants and products as the photocatalytic reaction is under operation. Fig. 3 implies the surface morphology of composite films before and after thermal-evaporated BiI_3. Fig. 3(a)–(c) show an obvious aggregation of either Ag NPs or Au NPs as they are deposited onto the CNF substrates through vacuum filtration. After the thermal evaporation of BiI_3 onto as-deposited NPs, their morphology significantly changes from spherical shape to flaky shape as shown in Fig. 3(d)–(f). With the interference of exotic Au NPs, the morphology of target films shows flaky shape with random orientation. That can be ascribed to different formation energy of SBI under different exposure condition, contact condition between BiI_3 and Ag NPs. Although large grain size facilitates carrier transportation, the low contact area between catalyst and reactants might hinder its photocatalytic activity.

Furthermore, the optical properties of thin film photocatalysts can determine the usage of incident light. Fig. 4(a) demonstrates the absorption spectrum of the free-standing substrate of CNF, control catalyst film, SBI/CNF, and two target catalyst films, SBI/Au/CNF and SBI-Au/CNF. The exotic Au NPs are speculated to induce Local Surface Plasma Resonance (LSPR) effect. Such effect harvests an incident light with a similar resonance frequency of oscillation electrons. Hot carriers with high energy have preference to stay onto plasmonic metal and facilitate the carrier separation [40,41]. That rationally speculates the LSPR effect is beneficial to the photocatalytic CO_2 reduction.

As an amorphous material, the free-standing CNF film shows superior transmission properties in visible light. The appearance of such films is shown in Fig. 4(b). An obvious absorption edge in the control film can be observed at around 680 nm, which is consistence with the bandgap of SBI. The target film of SBI/Au/CNF holds the superior absorption property in the series. It can be attributed to the bilayer microstructure

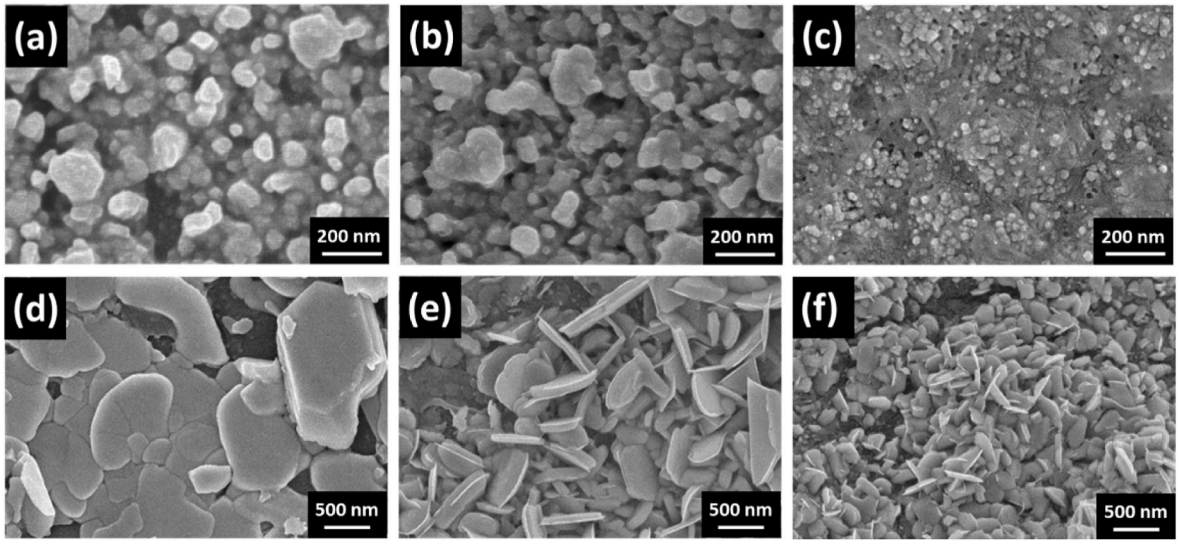

Fig. 3. FESEM images for various composite films: **(a–c)** composite/CNF before and **(*d*–f)** after BiI_3 thermal evaporation. **(a, d)** SBI/CNF, **(b, e)** SBI/Au/CNF, and **(c, f)** SBI-Au/CNF composite films.

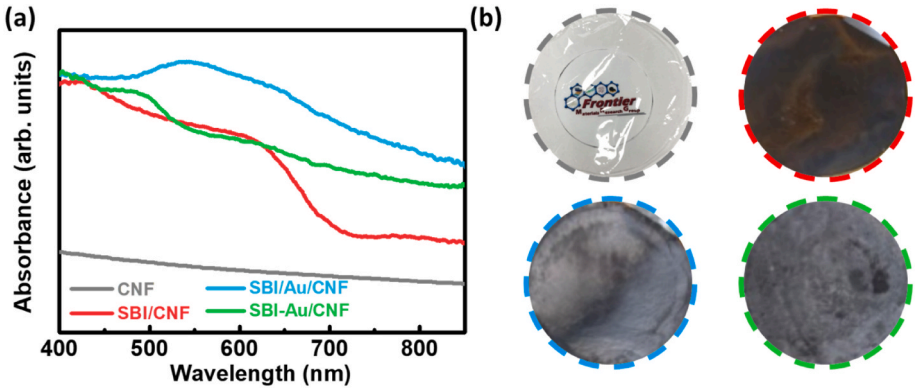

Fig. 4. Optical properties of different architectures: **(a)** Uv–vis absorption spectra and **(b)** digital photograph of the CNF, SBI/CNF, SBI/Au/CNF, and SBI-Au/CNF composite films.

of SBI/Au. The beneath layer of Au NPs acts as a scattering layer and helps to harvest much incident light. The other target film of SBI-Au/CNF shows similar absorption in short wavelength but a strong absorption at around 500 nm. This strong absorption is originated from the LSPR of Au NPs. The lateral scattering effect in both target films enhances the absorption harvesting in long wavelength incident light from 700 nm to 800 nm compared to the control film.

The improved optical properties of target films are speculated to promote their photocatalytic activity. Fig. S2 demonstrates the distribution of photocatalytic CO_2 reduction from each photocatalysis. The small distribution of CO yield from different batches infers that such composite films have high reproducibility and reliability. Fig. 5(a) summarizes the highest photocatalytic activity of control and target catalyst films for CO_2 reduction from the reliability test. Although the highest absorption ability of target film of SBI/Au/CNF has, it shows the lowest photocatalytic CO reduction yield. That can be attributed to the effect of Au NPs. The Au NPs serve as a light scattering layer and a carrier collection center for the composite. Even though the electron-hole pairs can be effectively separated with Au NPs, their location beneath the SBI layer hinders them from contacting the reactant molecule of CO_2 directly. Once the occurrence between CO_2 and Au NPs decreases, the excited electrons are hard to transfer to CO_2 and difficult to process reduction. In contrast, the SBI-Au/CNF film shows a superior CO production yield, enhancing around three times, to the control film. That can be ascribed to effective carrier separation and exposed active sites of Au NPs on the composite film. The proposed CO_2 reduction mechanism are listed as follow in Equation (1)–(4).

$$SBI - Au \xrightarrow{h\nu} h^+_{SBI} + e^-_{SBI} \quad (1)$$

$$e^-_{SBI-Au} \rightarrow e^-_{Au} \quad (2)$$

$$H_2O \rightarrow H^+ + OH^- \quad (3)$$

$$4h^+_{SBI} + 4OH^- \rightarrow O_2 + 2H_2O \quad (4)$$

$$CO_{2(ads)} + 2e^- + 2H^+ \rightarrow CO + H_2O \quad (5)$$

As the incident light that energy being higher than energy bandgap of an SBI strikes onto an SBI-Au film, electrons excite from the valence band of SBI to its conduction band and leaving the same number of holes (Equation (1)). Owing to high Schottky barrier between Au NPs and SBIs, the excited electrons prefer to stay at Au NPs once they migrate to Au NPs (Equation (2)). Neighboring water molecules dissociate to hydrogen ions and hydroxide ions (Equation (3)). The released hydroxide ions receive excited holes and reduce themselves to oxygen molecules and water moelcules (Equation (4)). Adsorbed CO_2 molecules ($CO_{2(ads)}$) thereafter react with hydrogen ions and excited electrons and generate carbon monoxide and water molecules (Equation (5)) [42]. Generally, carbon monoxide is considered as a molecule that annihilate active sites of a catalysis. To evaluate the photocatalytic activity stability of SBI-Au films, a 72 h of CO_2 reduction tests are carried out and shown in Fig. 5(b). The result reveals that SBI-Au/CNF has high stability for long-term photocatalytic reactions and has a CO reduction yield of 1500 μmol/g.

The film thickness of SBI-Au/CNF composite has been also examined from cross-sectional FE-SEM image, see in Fig. S3(a) and **(b)**. The intimate contact between CNF substrate and SBI-Au photocatalyst infers a good compatibility between them, and the averaged thickness of the composite film is 5.23 μm with a standard deviation of 0.23 μm. Although consistence increased yield of CO within 72 h indicates that such a composite film holds a good stability and reliability for photocatalytic CO_2 reduction, the crystal structure possibly changes to other phases after subjecting in such surrounding. It inspires us to observe the its crystal structure after photocatalytic CO_2 reduction to evaluate the stability in a microstructure point of view. Fig. S4 reveals crystal structure of the SBI-Au/CNF film before and after it conducts

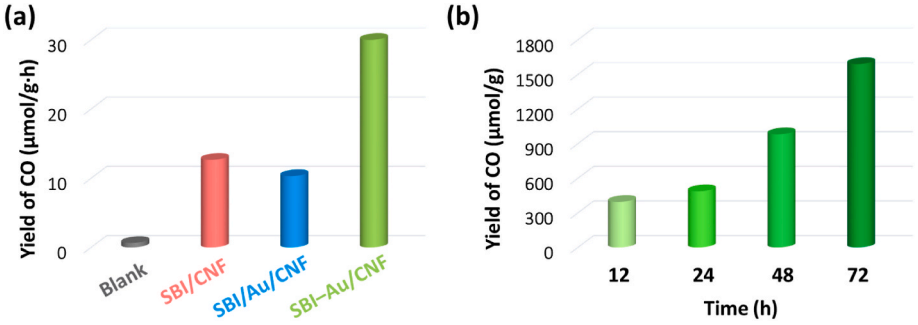

Fig. 5. Photocatalytic activity of SBI composite films for CO_2 reduction: **(a)** CO_2 photoreduction performance using various SBI/CNF composite films and **(b)** long-term performance test of SBI-Au/CNF for CO_2 reduction.

photocatalytic CO_2 reduction. The consistence characteristic peaks from plane (104), (009), and (110) of SBI can still be observed at both SBI-Au/CNF films. Also, the characteristic peak of Au NPs shows mere different. Both of XRD patterns are indicative of a stable crystal structure of an SBI-Au/CNF composite film. Fig. S5 demonstrates surface morphology of SBI-Au/CNF composite films, including fresh (Fig. S5(a)), two-year storage film (Fig. S5(b)), and two-year stored film after processing photocatalytic CO_2 reduction (Fig. S5(c)). The morphology shows mere different. That again proves that SBI-Au/CNF composite films hold excellent stability even they are stored in air for over two years. The consistence morphology in the composite film before and after photocatalytic CO_2 reduction again indicates such a photocatalyst has stable material property and can be applied in a long-term photocatalytic reaction.

4. Conclusion

In this study, composite films consisting of silver bismuth iodide were successfully fabricated using a simple two-step deposition process. By varying the stacking of the materials, a series of composite films were produced: SBI/CNF, SBI/Au/CNF, and SBI-Au/CNF. The SBI-Au/CNF composite film showed the highest photocatalytic activity for CO_2 reduction, with a yield of 31.96 μmol/g h, due to its superior light management and carrier communication path. The stability of SBI-Au/CNF was also demonstrated in long-term reaction conditions, showing stable reactivity for CO_2 reduction. This work highlights the potential of immobilized SBI materials and induced nanoparticles in improving light management, and provides versatile roles for metal nanoparticles in designing high-performance photocatalyst platforms for CO_2 reduction.

Credit author statement

Yi-Jing Lu and Jia-Mao Chang: Investigation. Yin-Hsuan Chang, Kai-Chi Hsiao, and Ting-Han Lin: Investigation, Writing- Original draft preparation. Ming-Chung Wu, Kai-Hsiang Hsu, Jen-Fu Hsu, and Kun-Mu Lee: Conceptualization, Methodology, Writing - Review & Editing, Funding acquisition, Supervision.

Declaration of competing interest

The authors declare that they have no known competing financial interests or personal relationships that could have appeared to influence the work reported in this paper.

Data availability

Data will be made available on request.

Acknowledgement

The authors appreciate Dr. Ming-Tao Lee (BL-13A1), Dr. Jyh-Fu Lee (BL-17C1) and Dr. Ting-Shan Chan (BL-01C1) at National Synchrotron Radiation Research Centre for useful discussion and suggestions, and Miss Y.-M. Chang at Instrumentation Centre of National Tsing Hua University for TEM analysis. The authors also thank the Microscopy Center at Chang Gung University for technical assistance. The financial support from National Science and Technology Council, Taiwan (Project No. 111-2628-E-182-001-MY2, and 111-2221-E-182-040-MY3), Chang Gung University (QZRPD181) and Chang Gung Memorial Hospital at Linkou (CMRPD2L0072 and BMRPC74) are highly appreciated.

Appendix A. Supplementary data

Supplementary data to this article can be found online at https://doi.org/10.1016/j.mssp.2023.107505.

References

[1] Y. Bo, C. Gao, Y. Xiong, Recent advances in engineering active sites for photocatalytic CO_2 reduction, Nanoscale 12 (23) (2020) 12196–12209.
[2] C. Gao, J.X. Low, R. Long, T.T. Kong, J.F. Zhu, Y.J. Xiong, Heterogeneous single-atom photocatalysts: fundamentals and applications, Chem. Rev. 120 (21) (2020) 12175–12216.
[3] Z. Otgonbayar, Y. Liu, K.Y. Cho, C.-H. Jung, W.-C. Oh, Novel ternary composite of $LaYAgO_4$ and TiO_2 united with graphene and its complement: photocatalytic performance of CO_2 reduction into methanol, Mater. Sci. Semicond. Process. 121 (2021), 105456.
[4] C. Hu, X. Chen, J. Low, Y.-W. Yang, H. Li, D. Wu, S. Chen, J. Jin, H. Li, H. Ju, C.-H. Wang, Z. Lu, R. Long, L. Song, Y. Xiong, Near-infrared-featured broadband CO_2 reduction with water to hydrocarbons by surface plasmon, Nat. Commun. 14 (1) (2023) 221.
[5] J. Fu, K. Liu, K. Jiang, H. Li, P. An, W. Li, N. Zhang, H. Li, X. Xu, H. Zhou, D. Tang, X. Wang, X. Qiu, M. Liu, Graphitic carbon nitride with dopant induced charge localization for enhanced photoreduction of CO_2 to CH_4, Adv. Sci. 6 (18) (2019), 1900796.
[6] J. Low, B. Cheng, J. Yu, Surface modification and enhanced photocatalytic CO_2 reduction performance of TiO_2: a review, Appl. Surf. Sci. 392 (2017) 658–686.
[7] X. Wang, C. Gao, J. Low, K. Mao, D. Duan, S. Chen, R. Ye, Y. Qiu, J. Ma, X. Zheng, R. Long, X. Wu, L. Song, J. Zhu, Y. Xiong, Efficient photoelectrochemical CO_2 conversion for selective acetic acid production, Sci. Bull. 66 (13) (2021) 1296–1304.
[8] W.-J. Ong, L.K. Putri, A.R. Mohamed, Rational design of carbon-based 2D nanostructures for enhanced photocatalytic CO_2 reduction: a dimensionality perspective, Chem. Eur J. 26 (44) (2020) 9710–9748.
[9] J. Fu, K. Jiang, X. Qiu, J. Yu, M. Liu, Product selectivity of photocatalytic CO_2 reduction reactions, Mater. Today 32 (2020) 222–243.
[10] Y. Wang, E. Chen, J. Tang, Insight on reaction pathways of photocatalytic CO_2 conversion, ACS Catal. 12 (12) (2022) 7300–7316.
[11] J. Low, J. Ma, J. Wan, W. Jiang, Y. Xiong, Identification and design of active sites on photocatalysts for the direct artificial carbon cycle, Acc. Mater. Res. 3 (3) (2022) 331–342.
[12] W. Zhang, A.R. Mohamed, W.-J. Ong, Z-scheme photocatalytic systems for carbon dioxide reduction: where are we now? Angew. Chem., Int. Ed. 59 (51) (2020) 22894–22915.
[13] Ž. Kovačič, B. Likozar, M. Huš, Photocatalytic CO_2 reduction: a review of Ab initio mechanism, kinetics, and multiscale modeling simulations, ACS Catal. 10 (24) (2020) 14984–15007.
[14] N. Podrojková, V. Sans, A. Oriňak, R. Oriňaková, Recent developments in the modelling of heterogeneous catalysts for CO_2 conversion to chemicals, ChemCatChem 12 (7) (2020) 1802–1825.
[15] W. Jiang, H. Loh, B.Q.L. Low, H. Zhu, J. Low, J.Z.X. Heng, K.Y. Tang, Z. Li, X. J. Loh, E. Ye, Y. Xiong, Role of oxygen vacancy in metal oxides for photocatalytic CO_2 reduction, Appl. Catal. B Environ. 321 (2023), 122079.
[16] J. Ma, R. Long, D. Liu, J. Low, Y. Xiong, Defect engineering in photocatalytic methane conversion, Small.Struct 3 (1) (2022), 2100147.
[17] Y. Shi, G. Zhan, H. Li, X. Wang, X. Liu, L. Shi, K. Wei, C. Ling, Z. Li, H. Wang, C. Mao, X. Liu, L. Zhang, Simultaneous manipulation of bulk excitons and surface defects for ultrastable and highly selective CO_2 photoreduction, Adv.Mater 33 (38) (2021), 2100143.
[18] J. Wang, Z. Wang, J. Zhang, S.-P. Chai, K. Dai, J. Low, Surface-active site modulation of the S-scheme heterojunction toward exceptional photocatalytic performance, Nanoscale 14 (48) (2022) 18087–18093.
[19] Z. Zhao, Z. Wang, J. Zhang, C. Shao, K. Dai, K. Fan, C. Liang, Interfacial chemical bond and oxygen vacancy-enhanced In_2O_3/CdSe-DETA s-scheme heterojunction for photocatalytic CO_2 conversion, Adv. Funct. Mater. (2023), 2214470.
[20] X. Li, J. Zhang, Y. Huo, K. Dai, S. Li, S. Chen, Two-dimensional sulfur- and chlorine-codoped g-C_3N_4/CdSe-amine heterostructures nanocomposite with effective interfacial charge transfer and mechanism insight, Appl. Catal. B Environ. 280 (2021), 119452.
[21] T. Hu, K. Dai, J. Zhang, S. Chen, Noble-metal-free Ni_2P modified step-scheme $SnNb_2O_6$/CdS-diethylenetriamine for photocatalytic hydrogen production under broadband light irradiation, Appl. Catal. B Environ. 269 (2020), 118844.
[22] A. Velasco-Hernández, R.A. Esparza-Muñoz, F.J. de Moure-Flores, J. Santos-Cruz, S.A. Mayén-Hernández, Synthesis and characterization of graphene oxide-TiO_2 thin films by sol-gel for photocatalytic applications, Mater. Sci. Semicond. Process. 114 (2020), 105082.
[23] Q. Wang, J. Warnan, S. Rodríguez-Jiménez, J.J. Leung, S. Kalathil, V. Andrei, K. Domen, E. Reisner, Molecularly engineered photocatalyst sheet for scalable solar formate production from carbon dioxide and water, Nat. Energy 5 (9) (2020) 703–710.
[24] L.I. Ibarra-Rodriguez, L.F. Garay-Rodríguez, L.M. Torres-Martínez, Photocatalytic reduction of CO_2 over $LaMO_3$ (M: Fe, Co, Mn)/Cu_xO films, Mater. Sci. Semicond. Process. 139 (2022), 106328.
[25] A. Isogai, Development of completely dispersed cellulose nanofibers, Proc.Jpn. Acad., Ser.B 94 (4) (2018) 161–179.
[26] Y. Chen, L. Zhang, Y. Yang, B. Pang, W. Xu, G. Duan, S. Jiang, K. Zhang, Recent progress on nanocellulose aerogels: preparation, modification, composite fabrication, applications, Adv.Mater 33 (11) (2021), 2005569.
[27] R.M. Cherian, A. Tharayil, R.T. Varghese, T. Antony, H. Kargarzadeh, C.J. Chirayil, S. Thomas, A review on the emerging applications of nano-cellulose as advanced coatings, Carbohydr. Polym. 282 (2022), 119123.

[28] Y. Nakamura, Y. Ono, T. Saito, A. Isogai, Characterization of cellulose microfibrils, cellulose molecules, and hemicelluloses in buckwheat and rice husks, Cellulose 26 (11) (2019) 6529–6541.
[29] T.-Y. Yu, Y.-K. Tseng, T.-H. Lin, T.-C. Wang, Y.-H. Tseng, Y.-H. Chang, M.-C. Wu, W.-F. Su, Effect of cellulose compositions and fabrication methods on mechanical properties of polyurethane-cellulose composites, Carbohydr. Polym. 291 (2022), 119549.
[30] P.-H. Chen, H.-C. Liao, S.-H. Hsu, R.-S. Chen, M.-C. Wu, Y.-F. Yang, C.-C. Wu, M.-H. Chen, W.-F. Su, A novel polyurethane/cellulose fibrous scaffold for cardiac tissue engineering, RSC Adv. 5 (9) (2015) 6932–6939.
[31] A.S.M. Wittmar, Q. Fu, M. Ulbricht, Photocatalytic and magnetic porous cellulose-based nanocomposite films prepared by a green method, ACS Sustainable Chem. Eng. 5 (11) (2017) 9858–9868.
[32] U.M. Garusinghe, V.S. Raghuwanshi, W. Batchelor, G. Garnier, Water resistant cellulose-titanium dioxide composites for photocatalysis, Sci. Rep. 8 (1) (2018) 2306.
[33] Y. Peng, H. Zhou, Y. Wu, Z. Ma, R. Zhang, H. Tu, L. Jiang, A new strategy to construct cellulose-chitosan films supporting Ag/Ag_2O/ZnO heterostructures for high photocatalytic and antibacterial performance, J. Colloid Interface Sci. 609 (2022) 188–199.
[34] T.-H. Lin, Y.-H. Liao, K.-M. Lee, Y.-H. Chang, K.-H. Hsu, J.-F. Hsu, M.-C. Wu, Organic solvent resistant nanocomposite films made from self-precipitated Ag/TiO_2 nanofibers and cellulose nanofiber for harmful volatile organic compounds photodegradation, Adv. Mater. Interfac. 8 (22) (2021), 2101467.
[35] D. Wu, X. Zhao, Y. Huang, J. Lai, H. Li, J. Yang, C. Tian, P. He, Q. Huang, X. Tang, Lead-free perovskite Cs_2AgBiX_6 nanocrystals with a band gap funnel structure for photocatalytic CO_2 reduction under visible light, Chem. Mater. 33 (13) (2021) 4971–4976.
[36] A.A. Ramachandran, B. Krishnan, D.A.A. Leal, E.G. Martinez, J.A.A. Martinez, D. A. Avellaneda, S. Shaji, Ag_2BiI_5 perovskite thin films: studies on structure, morphology, composition and optoelectronic properties for visible photodetector application, Mater. Today Commun. 24 (2020), 101092.
[37] M.-C. Wu, C.-H. Lin, T.-H. Lin, S.-H. Chan, Y.-H. Chang, T.-F. Lin, Z. Zhou, K. Wang, C.-S. Lai, Ultrasensitive detection of volatile organic compounds by a freestanding aligned Ag/CdSe-CdS/PMMA texture with double-side UV-ozone treatment, ACS Appl. Mater. Interfaces 11 (37) (2019) 34454–34462.
[38] L. Polavarapu, K.K. Manga, H.D. Cao, K.P. Loh, Q.-H. Xu, Preparation of conductive silver films at mild temperatures for printable organic electronics, Chem. Mater. 23 (14) (2011) 3273–3276.
[39] J. Turkevich, P.C. Stevenson, J. Hillier, A study of the nucleation and growth processes in the synthesis of colloidal gold, Discuss. Faraday Soc. 11 (0) (1951) 55–75.
[40] X. Zhang, X. Li, M.E. Reish, D. Zhang, N.Q. Su, Y. Gutiérrez, F. Moreno, W. Yang, H. O. Everitt, J. Liu, Plasmon-enhanced catalysis: distinguishing thermal and nonthermal effects, Nano Lett. 18 (3) (2018) 1714–1723.
[41] A. Furube, L. Du, K. Hara, R. Katoh, M. Tachiya, Ultrafast plasmon-induced electron transfer from gold nanodots into TiO_2 nanoparticles, J. Am. Chem. Soc. 129 (48) (2007) 14852–14853.
[42] Z.-x. Bi, R.-t. Guo, X. Hu, J. Wang, X. Chen, W.-g. Pan, Research progress on photocatalytic reduction of CO_2 based on LDH materials, Nanoscale 14 (9) (2022) 3367–3386.